SUPPRESSING THE LOW-FREQUENCY NOISE IN REVERSE-TIME MIGRATION UTILIZING THE NON-REFLECTING WAVE EQUATION

LINGLI ZHANG[1], WENGUANG SHI[2], ZHENGGUO HOU[2], YUXIAO REN[1] and RUIRUI WANG[3]

[1] *Geotechnical and Structural Engineering Research Center, Shandong University, Jinan 250061, P.R. China. ryxchina@163.com*
[2] *Guangdong Yuehai Pearl River Delta Water Supply Co., Ltd., Shenzhen, Guangdong 518001, P.R. China.*
[3] *School of Civil Engineering, Shandong Jianzhu University, Jinan 250101, P.R. China.*

ABSTRACT

Zhang, L., Shi, W.G., Hou. Z.G., Ren, Y.X. and Wang, R.R., 2023. Suppressing the low-frequency noise in reverse-time migration utilizing the non-reflecting wave equation. *Journal of Seismic Exploration*. 32: 1-20.

As a high-precision geophysical imaging method, reverse-time migration (RTM) is widely used in seismic exploration. However, the imaging quality in RTM is susceptible to low-frequency noise, which is chiefly caused by unwanted cross-correlation of reflections. In order to remove the low-frequency noise, the non-reflecting wave equation can be introduced to RTM. On this basis, we propose an improved RTM method utilizing the non-reflecting wave equation to achieve low-frequency noise suppression in prestack acoustic RTM. Specifically, the non- reflecting wave equation is only used in the process reverse- time wavefield simulation, to take advantage of its ability of weakening reflections. Accordingly, abnormal imaging points attributable to reflections can be reduced. We evaluated the denoising effect through numerical examples including a simple layered model, a concave model, and the complicated Marmousi model. The results show that low-frequency noise can be effectively suppressed by introducing the non-reflecting wave equation into RTM. This improved RTM method can achieve better imaging with less low-frequency noise compared with conventional RTM method. Moreover, the improved RTM method ensures computational efficiency without increasing storage demands.

KEYWORDS: reverse-time migration, low-frequency noise, non-reflecting wave equation, denoising.

INTRODUCTION

Migration is one of the most popular imaging methods in the field of seismic exploration (Fowler, 1997). In recent years, reverse-time migration (RTM) has been developed rapidly owing to its excellent imaging accuracy. Because of utilizing full-wavefield information through the application of the two-way wave equation, RTM can handle the limitation of inclination angle in imaging well. Meanwhile, it can effectively image interfaces with strong changes in velocity, density and other physical properties (Yoon et al., 2004). The concept of RTM was first proposed in 1983 (Mcmechan, 1983; Whitmore, 1983; Baysal et al., 1983; Loewenthal et al., 1983). Later, Levin et al. (1983) discussed the principle of RTM and presented its procedure. Subsequently, many scholars studied it from various aspects (Wang, 2000; Symes, 2007; Foltinek et al., 2009, Dai et al., 2013; Araya et al., 2009; Chen et al., 2019). At present, RTM has realized the development from acoustic wave equation to elastic wave equation and then to viscoelastic wave equation (Chang et al., 1987; Zhu et al., 2017; Wang et al., 2018), from 2D numerical simulation to 3D field data processing (Lesage et al. 2008), from the study of isotropic media to anisotropic media (Fletcher et al. 2009), and from poststack data processing to prestack data processing (Karazincir et al., 2006; Chattopadhyay et al., 2008; Xu et al., 2010).

The implementation of RTM can be presented as three main key steps (Fisher et al., 1992): extrapolating the source wavefield forward in time based on the two-way wave equation, extrapolating the receiver wavefield inversely in time, and imaging using imaging conditions (Sava et al., 2006; Liu et al., 2007; Sava et al., 2008). Cross-correlation is an effective imaging condition. It is based on the principle of time-consistency (Claerbout, 1971). When applying the cross-correlation imaging condition (Kaelin et al., 2006; Youn et al., 2001), an imaging point exists irrespective of real or abnormal imaging points as long as the extracted imaging time is consistent. Abnormal imaging points described previously are often called low-frequency noise, which will seriously interfere with the quality of image and further interpretation of data (Valenciano et al., 2003).

Extensive efforts have been made to suppress low-frequency noise. They can be mainly divided into two categories (Guitton, 2005; Kang et al., 2012). The first is denoising during the application of imaging conditions. It can be realized by following means:

(1) Applying the Poynting vector to suppress low-frequency noise. When applying this denoising method, the choice of denoising angle based on empirical values may lead to some points that cannot be directly calculated. Such points will further limit the denoising effect. Moreover, this method realizes angle-domain imaging by extracting the angle information of source and receiver, which will significantly increase its computational complexity and storage requirement (Ren et al., 2015; Chen et al., 2014).

(2) Separating wavefield according to the direction of wavefield propagation to suppress low-frequency noise. In this approach, the wavefield is decomposed into up-, down-, right-, and left-going waves.

However, it is difficult to effectively separate traveling waves from different directions in complex geological structures. In addition, the calculation and storage costs will be significantly increased because the wavefield should be recorded from different directions separately at the same time. This may pose a big challenge in processing massive amounts of data (Wang et al., 2008; Mehta et al., 2007).

The second is denoising by filtering (Shapiro, 1970; Verschuur et al., 1997). It mainly includes high-pass filtering, least-squares filtering with prediction-error filters (Xue et al., 2016), fan filtering plus wavefield decomposition (Suh et al., 2009), and Laplace filtering (Liu et al., 2010). All filtering denoising methods have the common problem of losing effective amplitudes. As the common and effective filtering method (Kim et al., 2013), Laplace filtering has the common problem of the direct filtering method mentioned above. In addition, more serious high-frequency noise will be generated while suppressing low-frequency noise, which will affect the imaging quality of high-steep fault structures in complex areas.

In this study, we focus on suppressing low-frequency noise during wavefield propagation. In other words, reflections are suppressed by modifying the wave equation in reverse time wavefield propagation to achieve the final purpose of suppressing low-frequency noise. Some scholars have conducted research from different aspects aiming at suppressing reflections (Zhu et al., 1989; Wang et al., 1993; Wu et al., 2000). Baysal et al. (1984) firstly proposed the two-way non-reflecting wave equation, which can avoid interlayer reverberations. Du et al. proposed the forward simulation algorithm of staggered grid finite difference form based on non-reflecting wave equation, and applied it in embankment forward simulation (Du et al., 2002). Zhang et al. (2009) proposed a new non-reflecting recursive RTM algorithm to image ragged surface by introducing the wave-impedance function into the non-reflecting acoustic wave equation. However, these studies only explored the application of this method to post-stack data.

Inspired by them, the non-reflecting wave equation is introduced into acoustic RTM prestack data process to suppress low-frequency noise. In this paper, we present three representative simulating examples, including a simple layered model, a concave model, and the complicated Marmousi model, to illustrate the efficiency of this method.

METHOD

Acoustic reverse-time migration (RTM) is a common imaging method. This method can not only ensure certain imaging effects, but it is also relatively simple compared with the elastic wave method. At present, it has been widely used in practical production. The form of the full acoustic wave equation under inhomogeneous condition [eq. (1)], and the acoustic wave equation under constant density and isotropy condition [eq. (2)] are presented here.

$$\frac{1}{\rho v^2} \frac{\partial^2 P}{\partial t^2} = \frac{\partial}{\partial x}\left(\frac{1}{\rho}\frac{\partial P}{\partial x}\right) + \frac{\partial}{\partial z}\left(\frac{1}{\rho}\frac{\partial P}{\partial z}\right) \quad , \tag{1}$$

$$\frac{\partial^2 P}{\partial t^2} = v^2 \frac{\partial^2 P}{\partial x^2} + v^2 \frac{\partial^2 P}{\partial x^2} \quad , \tag{2}$$

where P denotes the pressure function; x and z represent the horizontal and vertical directions, respectively; ρ is the density of the medium; v is the velocity of acoustic wave in the medium; and t is the time variable.

Eq. (2) is the common wave equation describing the propagation characteristics of waves in seismic simulation. However, this equation will lead to strong reflections when waves meet the interface, which can further generate low-frequency noise in RTM. Therefore, an acoustic wave equation that can effectively suppress reflections of interface becomes the key in suppressing low-frequency noise in RTM.

Non-reflecting Wave Equation

Baysal et al. (1984) proposed the non-reflecting wave equation in order to describe the weak-reflection propagation characteristics of wavefield simulation. Firstly, the derivation of non-reflecting wave equation is shown here. Theoretically, reflections will not occur without physical differences. Here, we can simply interpret the physical properties as wave-impedance. In order to suppress reflection in theory, we can assume that media on both sides of the geological interface have the same wave-impedance. Then, the form of the non-reflecting wave equation can be easily obtained in eq. (4) by introducing the wave-impedance equation eq. (3) into full acoustic wave equation eq. (1).

$$\rho v = c \quad , \tag{3}$$

$$\frac{\partial^2 P}{\partial t^2} = v^2 \frac{\partial^2 P}{\partial x^2} + v^2 \frac{\partial^2 P}{\partial x^2} + \left(v\frac{\partial v}{\partial x}\left(\frac{\partial P}{\partial x}\right) + v\frac{\partial v}{\partial z}\left(\frac{\partial P}{\partial z}\right)\right) \quad , \tag{4}$$

where c is a constant representing the same wave-impedance.

Comparing the non-reflecting wave equation eq. (4) with the conventional acoustic wave equation eq. (2), it is obvious that an additional

term is added on the right side of the non-reflecting wave equation. This additional term provides the theoretical basis of weakening reflections during the wavefield simulation process. Taking velocity and stress as basic unknowns, the non-reflecting wave equation can be transformed to the form of the first-order velocity-stress equation shown in eq. (5). In particular, $V = \partial P/\partial t$ is the velocity variable, $\tau_x = v\dfrac{\partial P}{\partial x}$ and $\tau_z = v\dfrac{\partial P}{\partial z}$ are the equivalent stresses in the X- and Z-directions, respeτctively.

$$\begin{cases} \dfrac{\partial V}{\partial t} = v\dfrac{\partial \tau_x}{\partial x} + v\dfrac{\partial \tau_z}{\partial z} \\[2mm] \dfrac{\partial \tau_x}{\partial t} = v\dfrac{\partial V}{\partial x} \\[2mm] \dfrac{\partial \tau_z}{\partial t} = v\dfrac{\partial V}{\partial z} \end{cases} . \tag{5}$$

Improved RTM Based on Non-reflecting Wave Equation

Considering the ability of the non-reflecting wave equation to weaken reflections, we proposed the improved RTM method based on the non-reflecting wave equation. Specifically, the non-reflecting wave equation is applied in the reverse wavefield propagations of RTM to weaken reflections, and the low-frequency noise caused by the imaging of unwanted reflection is then suppressed. Here, the denoising mechanism of the improved RTM method based on the non-reflecting wave equation in imaging is presented.

For concrete imaging using RTM, we often use the cross-correlation imaging condition, which is based on the principle of the time-consistency criterion. For a fixed source and receiver array, all positions satisfying that the sum of forward time of the source and reverse time of the receiver is equal to the travel time, will be considered as real imaging points. Here, we introduce a horizontal layered model to explain the reason for the suppression of low-frequency noise by the non-reflecting wave equation in the RTM process.

As shown in Fig. 1, point A is the true imaging point representing the interface position, and B is one of the abnormal imaging points selected randomly. Abnormal points such as B will finally form what is often known as low-frequency noise. In order to distinguish the formation process of A and B, the corresponding path of B is shifted to the right slightly. Owing to the application of the non-reflecting wave equation, reflections from the interface, shown as the red dotted line in Fig. 1, will be suppressed. Naturally, the wrong imaging process shown in the dotted line will no longer exist, whereas the true imaging process shown by the solid line is retained. Other abnormal imaging points can be analogized to point B. Based on this, the suppression of low-frequency noise in RTM can be finally achieved. In an ideal case, the RTM method based on the non-reflecting wave equation images only points on the interface, which will make the imaging results clearer.
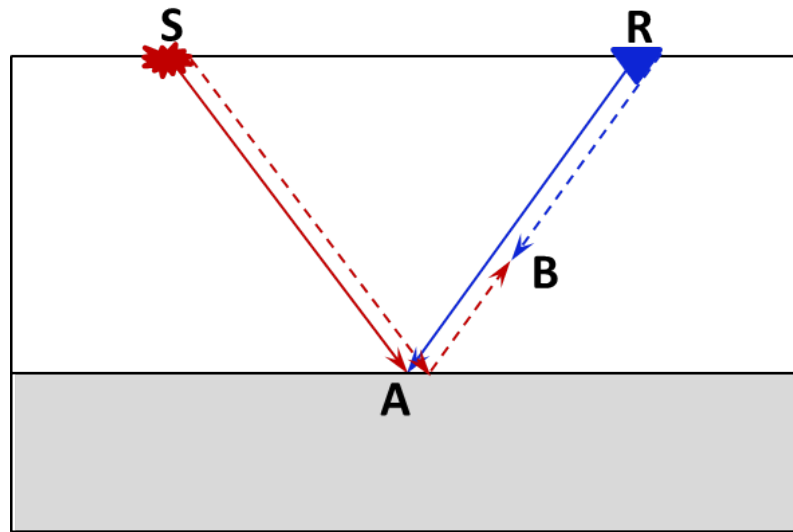

Fig. 1. Schematic diagram of low-frequency noise suppression. Point A is the correct imaging point. Point B is one of the abnormal imaging points selected randomly. S represents the source point. R represents the receiver. The gray line is the propagation path satisfying the time-consistency imaging criterion. The solid and dotted lines are the imaging processes of points A and B, respectively. The red and blue lines represent the forward propagation path excited by the source and receiver, respectively.

Absorbing Boundary Condition of Improved RTM

We also use the perfectly matched layer (PML) absorbing boundary condition to eliminate the interference of boundary reflections in the improved RTM. The PML absorbing boundary condition is a method proposed by Bérenger in electromagnetics (Bérenger et al., 2007). The basic principle of PML is to add a virtual anisotropic media around the calculation region. Then, the outgoing seismic wave can be absorbed by the outer boundary gradually. PML can satisfy the absorption effect of boundary reflections over a wide frequency band and large incident angle range. Moreover, it demands very limited storage and calculation costs (Drossaert et al., 2007; Zhang et al., 2010). The form of PML is given in eq. (6):

$$\begin{cases} \dfrac{\partial P}{\partial t} = v^2 \left(\dfrac{1}{\kappa_x} \dfrac{\partial \tau_x}{\partial x} + \psi_x \right) \\[2ex] \dfrac{\partial P}{\partial t} = v^2 \left(\dfrac{1}{\kappa_z} \dfrac{\partial \tau_z}{\partial z} + \psi_z \right) \\[2ex] \dfrac{\partial \tau_x}{\partial t} = \dfrac{1}{\kappa_x} \dfrac{\partial P}{\partial x} + \omega_x \\[2ex] \dfrac{\partial \tau_z}{\partial t} = \dfrac{1}{\kappa_z} \dfrac{\partial P}{\partial z} + \omega_z \end{cases} , \tag{6}$$

(6)

where ψ_j, τ_j, and ω_j are introduced as instrumental variables, and j represents the direction of x and z. Usually, we use the empirical value $\kappa_j = 1$. Other detailed information can be referred from the literature mentioned above.

Implementation of the Improved RTM

We proposed an improved RTM method that can weaken low-frequency noise. The non-reflecting wave equation is used in the reverse simulation of the receiver of RTM to weaken reflections. Furthermore, imaging results with less low-frequency noise can be obtained by using cross-correlation imaging conditions. Fig. 2 presents flow charts of the traditional and improved RTM methods. According to the figure, the improved RTM has appears to have fewer steps for implementation compared to the traditional RTM. In addition, the improved RTM can suppress low-frequency noise during the wavefield propagation, whereas the traditional RTM requires extra denoising steps, such as applying imaging conditions and post filtering. Here, we present the three main steps of the improved RTM method as follows:

(1) Forward modeling based on the traditional wave equation, recording the information matrix containing the characteristics of forward wavefield simultaneously;

(2) Simulating the reverse-time wavefield under the non-reflecting wave equation while recording the wavefield matrix;

(3) Applying cross-correlation conditions to obtain the final RTM imaging results with less low-frequency noise.
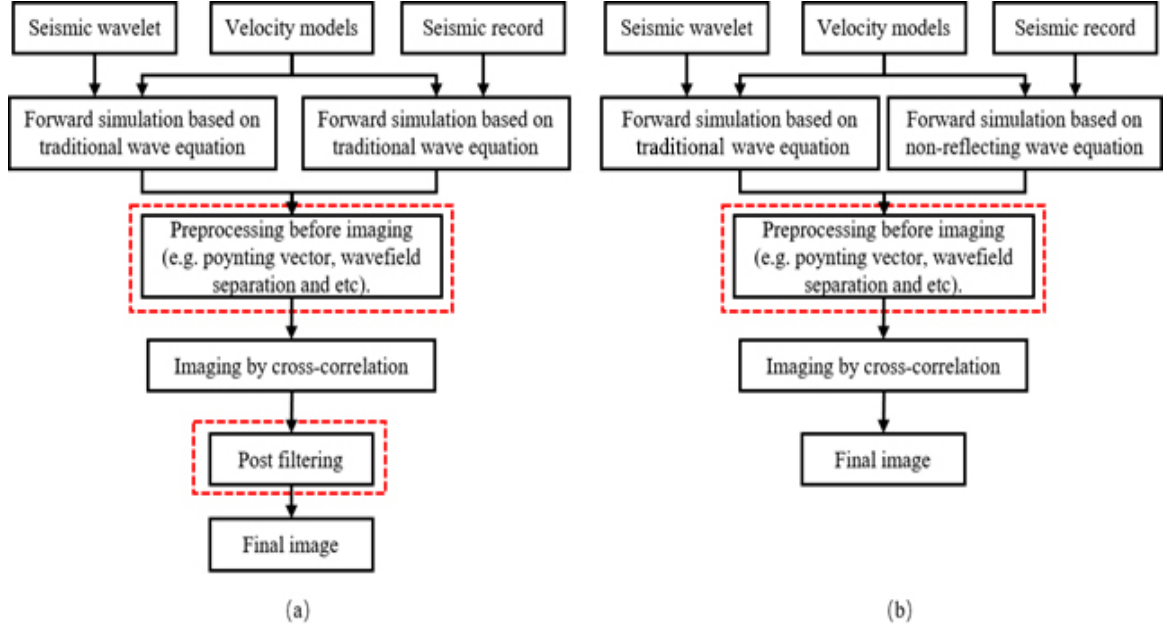
Fig. 2. Flow chart of RTM based on (a) the traditional and (b) non-reflecting acoustic wave equation. The red dotted frames denote the main denoising steps of the traditional RTM methods.

EXAMPLES

Simple Layered Model

We investigate the efficiency of low-frequency noise suppression of the improved RTM using a very simple two-layered model. As shown in Fig.3, the model has an upper velocity of 2000 m/s and a lower velocity of 3000 m/s. The Ricker wavelet with a peak frequency of 40 Hz is adopted here. The grid is set as 240×140 with a grid spacing of 2 m in both X- and Z-directions. The sampling interval is 0.2 ms and the recording length is 0.5s. A point source is set in the position of X = 240 m and Z = 2 m. To record the seismogram, 48 receivers are equally located at X = 0, 10, 20, 30 ..... 480 m and Z = 2 m. The PML boundary condition with a layer of 30 is applied to the numerical simulation of the model. Fig. 4(a) and Fig. 4(b) illustrate forward seismograms of the traditional and non-reflecting wave equations after muting direct waves. From the results, reflections are obviously suppressed for the improved RTM method. A single-trace seismic wavelet recorded by the 3st receiver is selected to quantitatively analyze the effect of the non-reflecting wave equation, which is shown in Fig. 5. The peak of positive amplitude based on the traditional acoustic wave equation is 0.013, while it is 0.003 for the non-reflecting forward simulation. Meanwhile, the peak negative amplitude of the reflected-wave based on the traditional acoustic wave equation is 0.01, while that of the non-reflecting forward simulation is 0.002. In other words, the peak amplitude could be reduced to about a quarter of the original peak amplitude by the applying non-reflecting wave equation. The comparison result of the two different forward simulation proves that the non-reflecting wave equation method can effectively suppress reflections.
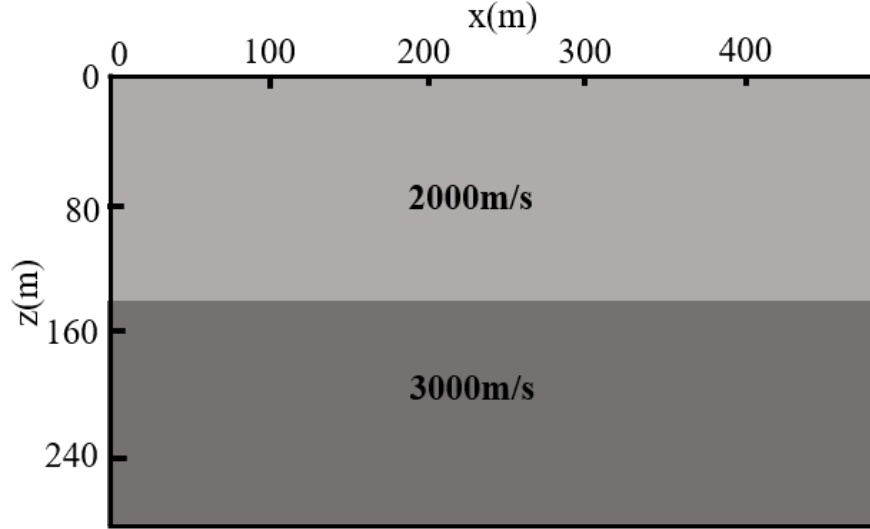
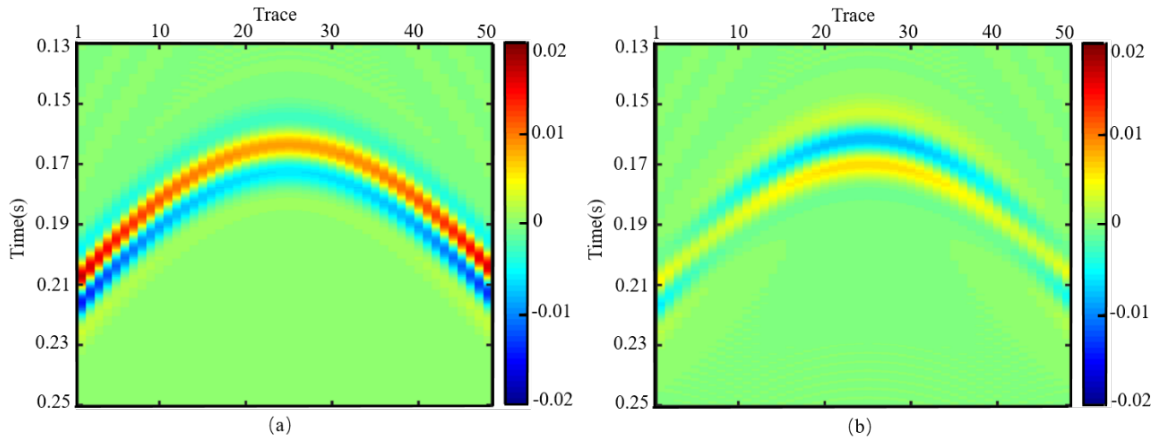Fig. 3. Velocity model used for modelling the simple horizontal structure.

Fig. 4. (a) Seismogram of conventional forward-simulation results for the layered model. (b) Seismogram of non-reflecting forward-simulation results for the layered model.

On the basis of forward simulation analysis for the simple layered model, RTM results based on different acoustic wave equations are discussed below. For better contrasting the denoising effect of conventional and improved RTM, we use the true velocity model as the initial model. Fig. 6(a) shows the imaging result of the traditional RTM method. Fig. 6(b) shows the imaging result of the improved RTM method. The results of both the conventional and improved RTM method clearly depict the location of the geological interface correctly. Intuitively, the two sides of the interface are not well displayed due to the limitation of the single source. However, the artefact area denoted by the red dotted box in Fig. 6(b) is much smaller than that in Fig. 6(a), especially in the area near the source point. Moreover, the improved RTM method facilitates seismic illumination (Kaelin et al. 2006). Indeed, the artifact area represents low-frequency noise.
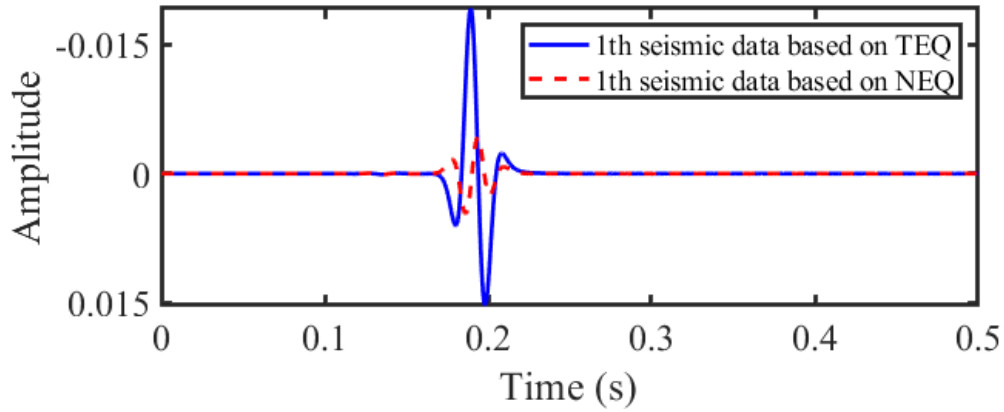
Fig. 5. Seismic record of Trace 3. The red dotted line and the blue solid line represent the results of the traditional and non-reflecting forward simulation, respectively. TEQ and NEQ stand for the traditional and non-reflecting acoustic wave equations, respectively.
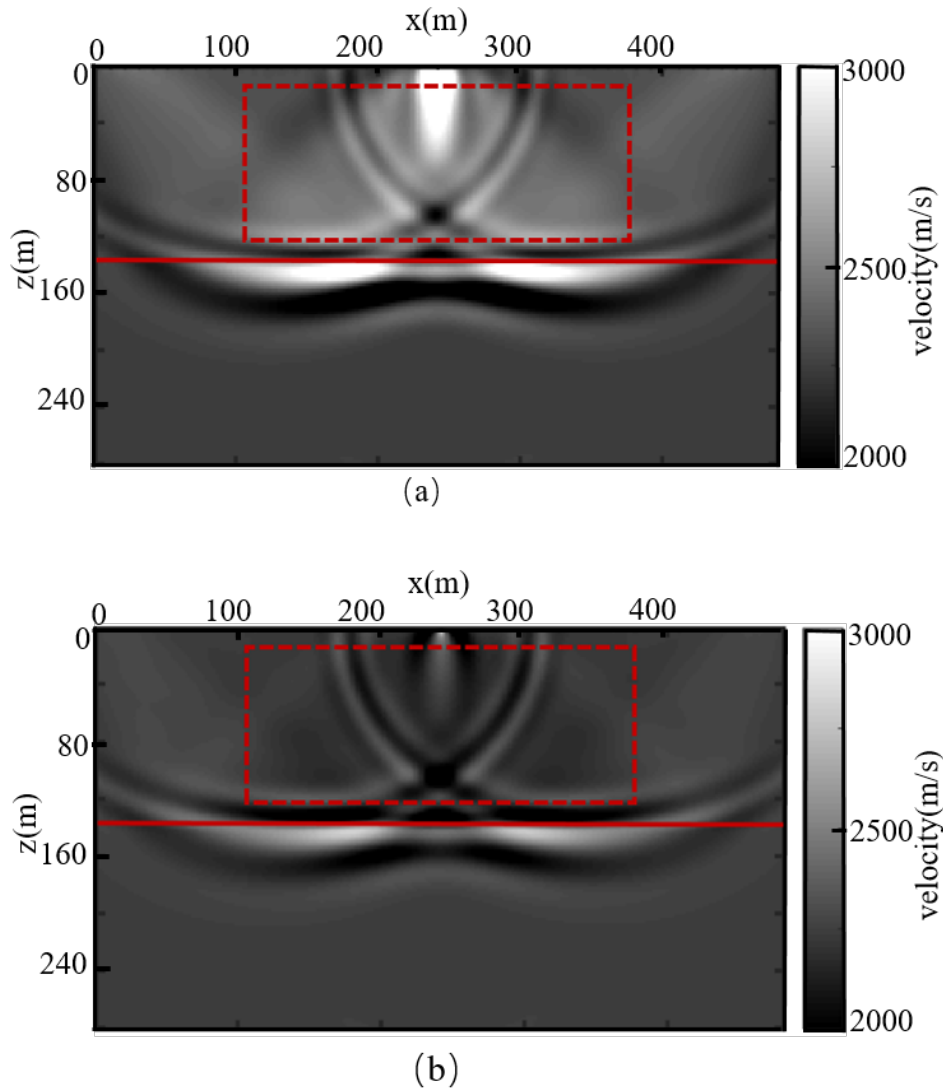

(a)

(b)

Fig. 6. Imaging results of the simple layered model using (a) the conventional RTM and (b) the improved RTM. The red dotted box denotes the low-frequency noise area. The red solid line denotes the interface between different media.

Through spectrum analysis, the imaging data are transformed from the time-domain to the frequency-domain, which can help explain the effect of low-frequency suppression. In the two-dimensional spectrum, the change in position from the surrounding area to the center represents the frequency change from high to low, and the color intensity from dark to light indicates the energy from strong to weak. Considering the two indicators, the low-frequency noise in Fig. 7(a) is stronger than that in Fig. 7(b). In addition, the intensity index of low-frequency noise (ILN) is introduced as a parameter to quantitatively analyzing low-frequency noise. The calculation principle of ILN is to transform the imaging data to the frequency domain through two-dimensional Fourier transformation. Low-pass filtering is then carried out according to empirical values. ILN is finally obtained through the calculation of two norm of the filtered imaging data. The value of ILN represents the intensity of low-frequency noise: the larger the value, the stronger the low-frequency noise. As shown in Table 1, the ILN values for the traditional RTM and improved RTM are 53.53 and 33.18, respectively. The results show that the low-frequency noise is weaker for the improved method than for the traditional method. According to the above analysis, we can finally draw the conclusion that the improved RTM is more effective in denoising.
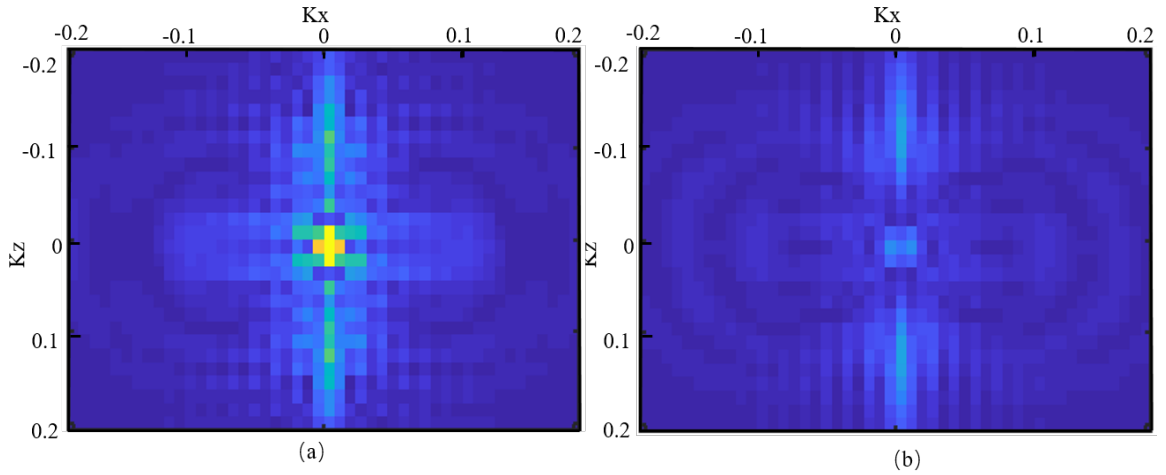

Fig. 7. (a) 2D Spectrum of conventional RTM imaging data for the layered model. (b) 2D Spectrum of improved RTM imaging data for the layered model. The Kx- and Kz-axes represent the normalized wavenumber in the x- and z-directions, respectively.

Concave Model

The denoising effectiveness of the improved RTM for imaging steep dips is also evaluated. A concave velocity model with a left inclination of 60 degree and a right inclination of 30 degree is introduced, whose size is 600×190 m, as shown in Fig. 8. The upper and lower velocities of the concave model are 2000 m/s and 3000 m/s, respectively. The source wavelet, sampling interval, grid size, and PML absorbing boundary condition are same as in the simple layered model. The recording length is set as 1 s, A single source is located at X = 300 m and Z = 2 m, and 60 receivers are evenly distributed by 10 m in the x-direction and located at Z = 2 m. The

forward simulation of the concave velocity model is performed firstly. Fig. 9(a) and Fig. 9(b) are seismograms of forward simulation based on the traditional acoustic wave equation and non-reflecting wave equation, respectively. The black, blue, and red arrows correspond to the seismogram of the reflections for the left inclined, lower horizontal, and right inclined interfaces, respectively. The only part of the seismograms with valid information is shown on the figure. In the seismograms, all reflections marked by arrows in Fig. 9(b) are suppressed better than those in Fig. 9(a). For clearly distinguishing the reflections from different interfaces, data of the 55th trace are selected for further comparative analysis. Fig. 10 illustrates the wavelet of the seismic data picked up by the 55th receiver. In the figure, reflections from the right inclined, lower horizontal, and left inclined interfaces marked by yellow, black, and green dotted frames are suppressed to varying degrees.
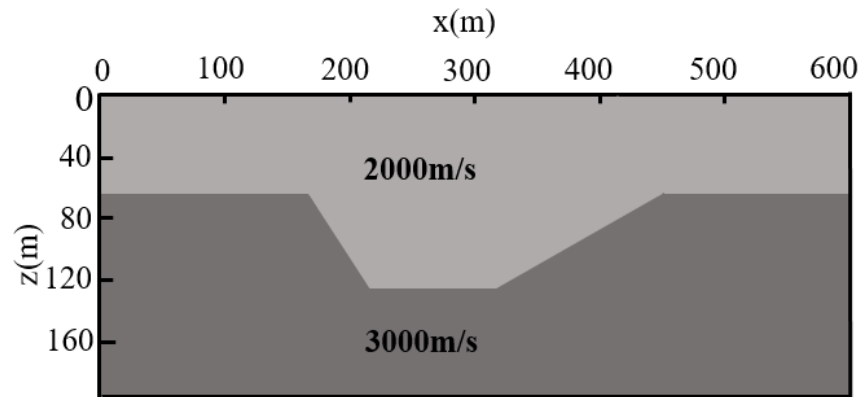

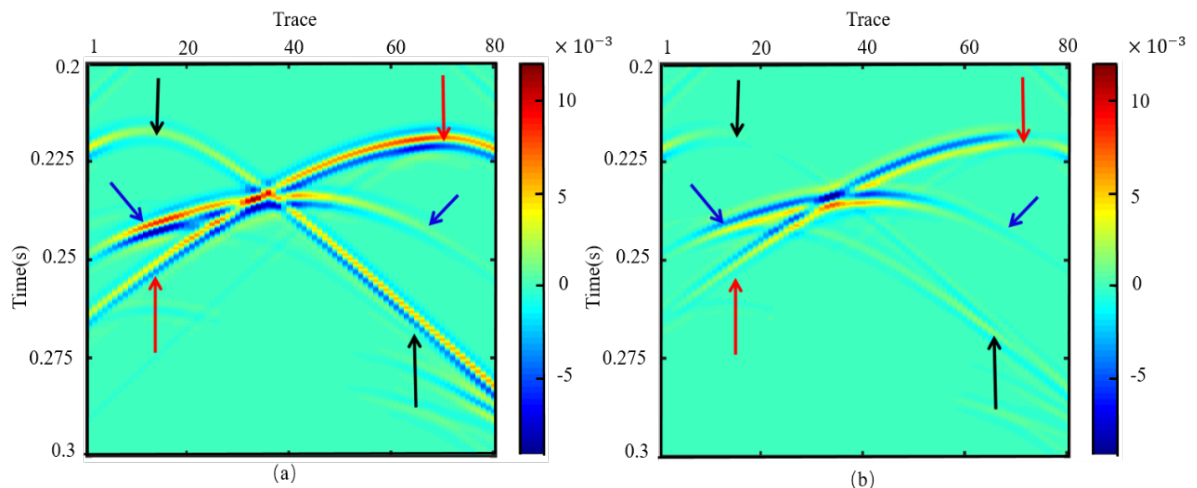Fig. 8. Velocity model used for modeling the concave structure.

Fig. 9.   (a) Seismogram of the conventional forward-simulation for the concave model. (b) Seismogram of the non-reflecting forward-simulation for the concave model. The red arrows denote reflections. The red, blue, and red arrows correspond to the seismograms of reflections for the left inclined, lower horizontal, and right inclined interfaces, respectively.
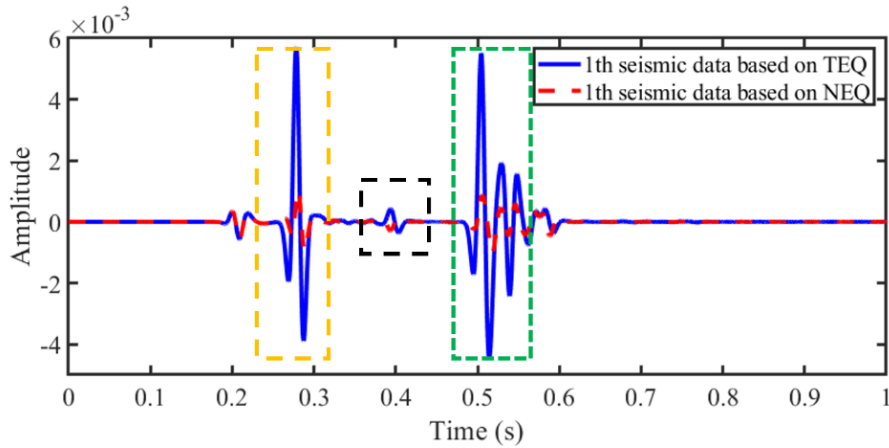
Fig. 10. Seismic record of Trace 55. The red dotted line and the blue solid line represent the results of the traditional and non-reflecting forward simulations, respectively. The yellow, black, and green dotted frames represent the wavelet of the right inclined, lower horizontal, and left inclined interfaces, respectively. TEQ and NEQ stand for the traditional and non-reflecting acoustic wave equations, respectively.

Fig. 11(a) and Fig. 11(b) show the imaging results of the traditional and improved RTM methods, when the true concave velocity model are considered as the initial model. Both methods achieved the generation of contour lines, which could be judged by comparing the imaging position with the actual interface shown by the black solid line. The artifact area of Fig. 11(b) denoted by the black arrows is smaller than that in Fig. 11(a), which can be mainly reflected in the location near the source point marked with black arrows and the groove area. Meanwhile, the intensity of low-frequency noise reflected by color scales in Fig. 11(b) is weaker than that in Fig. 11(a).
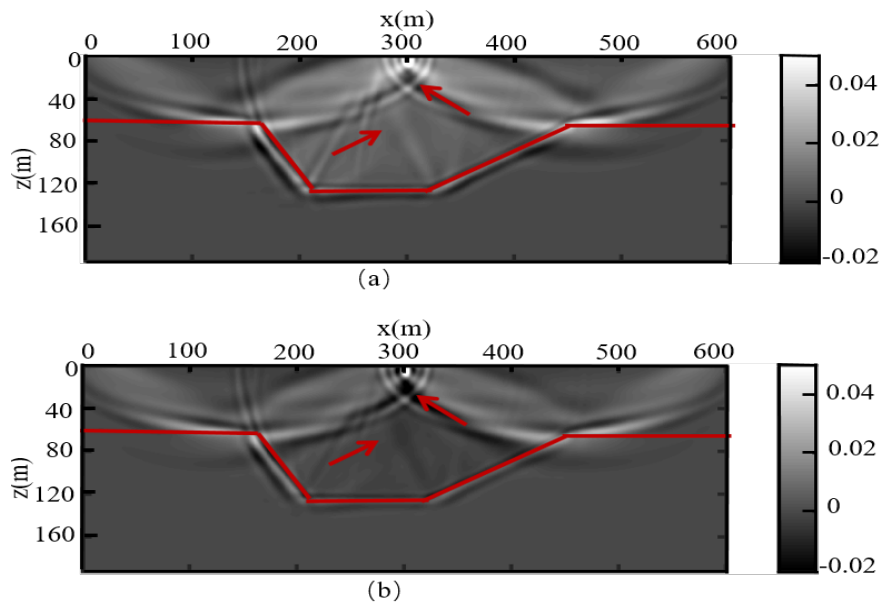

Fig. 11. Imaging results of the concave model using (a) the conventional RTM and (b) the improved RTM. The red arrows denote the area of low-frequency noise. The red solid line denotes the interface between different media.

In addition, 2D spectrum and ILN mentioned above are introduced to qualitatively and quantitatively analyze the intensity of low-frequency noise. The low-frequency noise range of the conventional RTM shown in Fig. 12(b) is smaller than that in Fig. 12(a). ILN of the improved RTM is 81.29, whereas that of the traditional RTM is 189.96, as shown in Table 1. The quantitative and qualitative comparison strongly proved the effectiveness of the improved RTM in both dip structure imaging and low-frequency noise suppression.
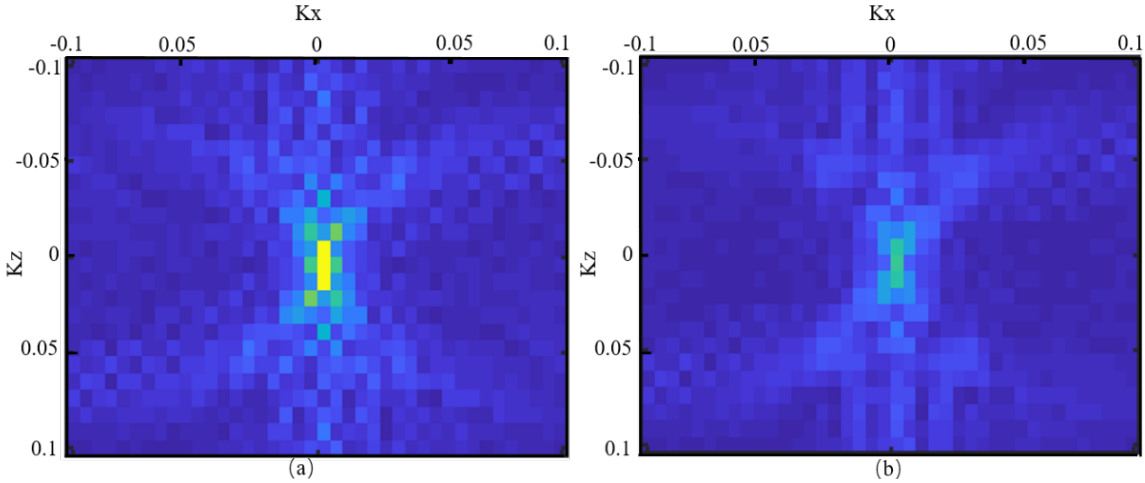

Fig. 12. (a) 2D Spectrum of conventional RTM imaging data for the concave model. (b) 2D Spectrum of improved RTM imaging data for the concave model. The Kx- and Kz-axes represent the normalized wavenumber in X- and Z-directions, respectively.

Marmousi Model

We test the denoising efficiency of the improved RTM method for complex geological models by introducing the Marmousi model (Bourgeois et al. 1990). The Original Marmousi model is resampled to the model space of 215 ×700 with velocity ranging from 1200 m/s to 4700 m/s, as shown in Fig. 13(a).

A wavelet source with a peak frequency of 20 Hz is adopted in the synthetic experiment. The grid size is   m, the time window is 2 s, and the time step is   s. We still use the true Marmousi velocity model to test the denoising effect for the low-frequency noise. 70 shots are eventually located at the top of the Marmousi model (z = 5 m). On the same horizontal line as the source, 140 receivers are equally distributed. The imaging artifacts caused by low-frequency noise in Fig. 13(b) is stronger than that in Fig. 13(c), especially in the area denoted by the red dashed box. For a clearer comparison, the enlarged view of the area marked by the red dashed box in Fig. 13(b) and Fig. 13(c) are given in Fig. 14(a) and Fig. 14(b), respectively. In Fig. 14(a), the imaging area is completely obscured by the imaging noise, which look like the dispersion of seismic record. In contrast, Fig. 14(b) is much clearer with a higher imaging resolution. Through above analysis, the

RTM method based on non-reflecting wave equation can overcome the imaging noise problem to a certain extent, which proves that the proposed method is also applicable to complex models.
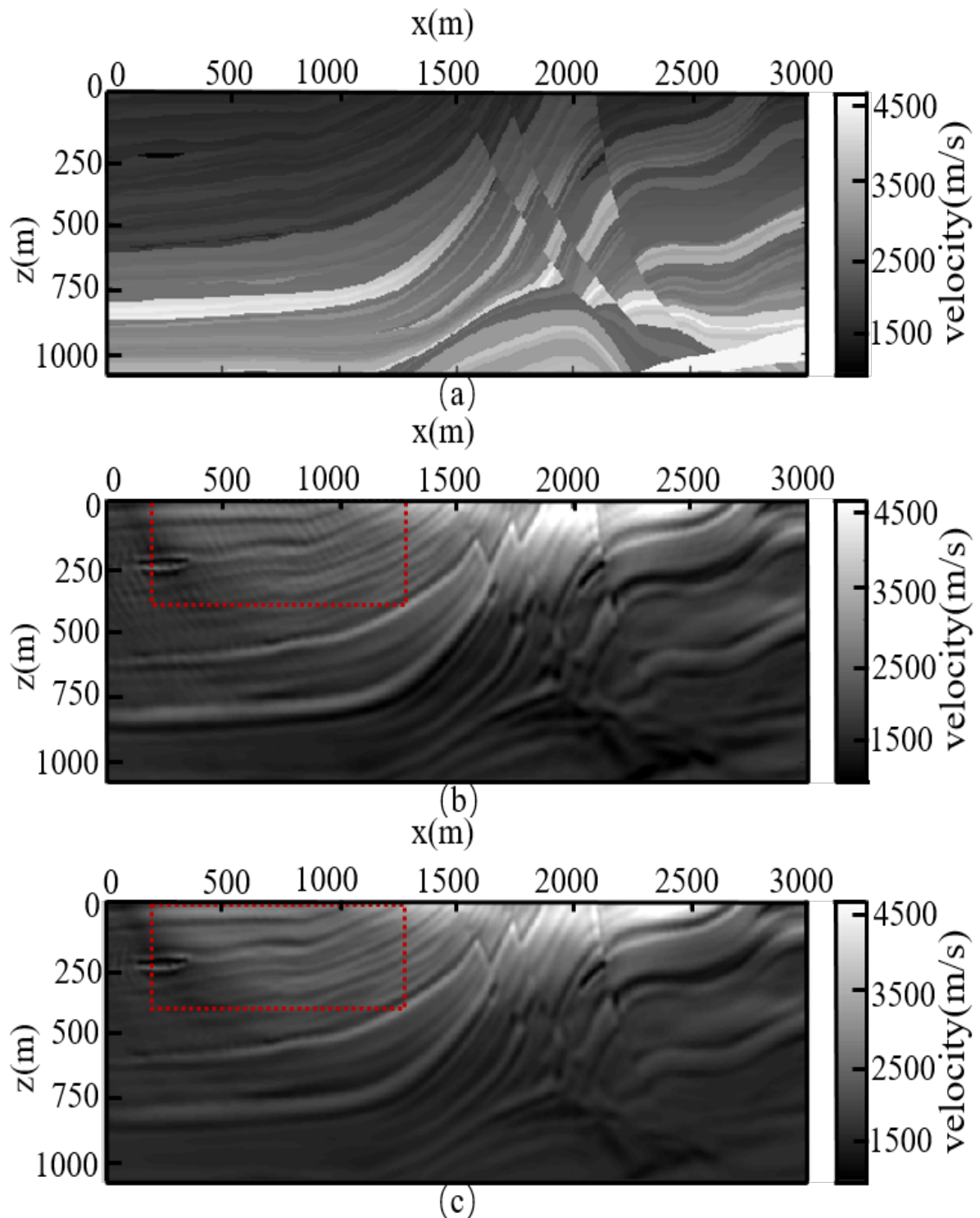

Fig. 13. (a) Marmousi velocity model. Imaging results of the simple layered model using (b) the conventional RTM and (c) the improved RTM.
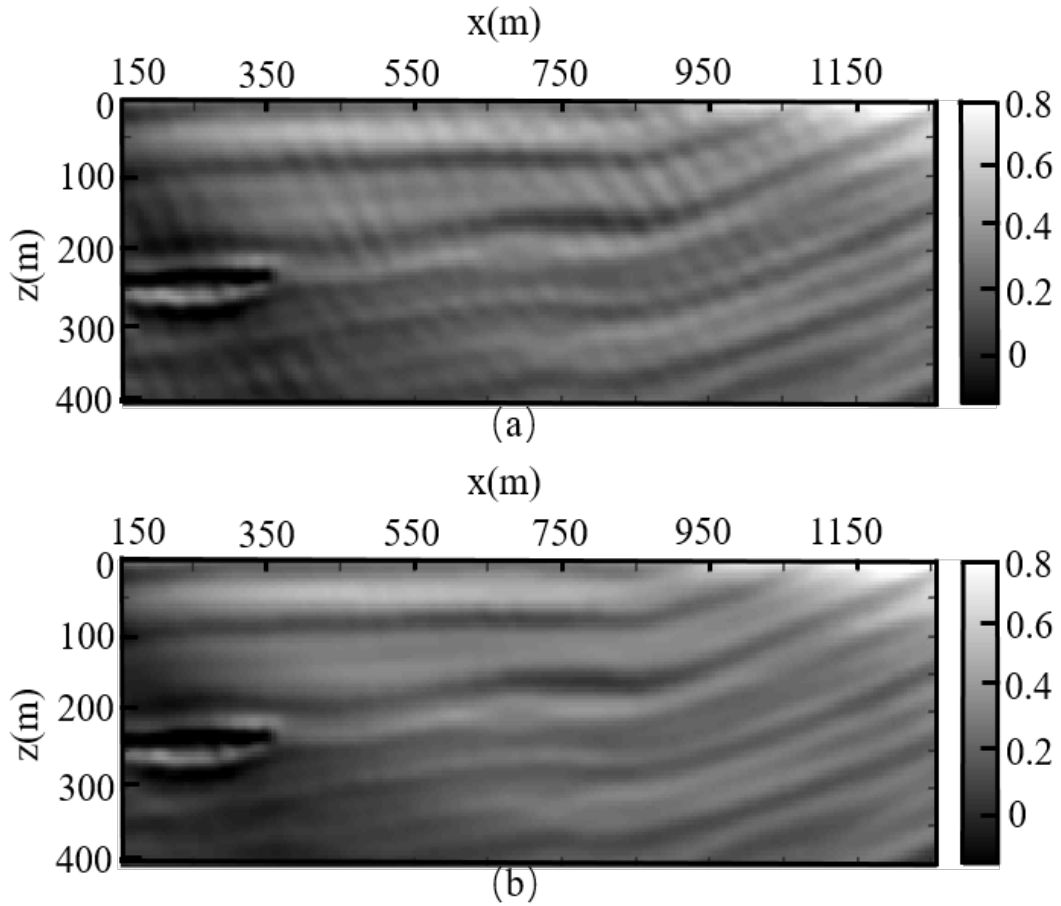
Fig. 14. The enlarged view of the area marked by the red dotted rectangle in (a) Fig. 13(b) and (b) Fig. 13(c).

In addition, we also adhibit parameter ILN described above to quantitatively analyze the intensity of low-frequency noise between the two RTM methods. Table1 shows ILN values of the two RTM methods. ILN of the improved method is only 66.68, whereas that of the traditional method reached 69.48. This further reveals the effectiveness of the improved RTM in suppressing low-frequency.

Table 1. ILN of traditional and improved RTM methods.

RTM	Layered Model	Concave	Marmousi Model
Traditiona	53.53	189.96	69.48
Improved	33.18	81.29	66.68

DISCUSSION

In this paper, we proposed an improved RTM method based on the non-reflecting wave equation. Through comparisons of imaging results of the layered, concave, and Marmousi models, the improved RTM was found to be advantageous over the traditional RTM method regarding low-frequency noise suppression. However, the imaging artifacts of low frequency noise could not be eliminated completely. Furthermore, the proposed method has several limitations.

The non-reflecting wave equation is derived on the assumption that the same wave-impedance means no reflection in theory. However, the assumption only exists in the case of vertical incidence or small incident angle. Therefore, when the incident angle is large, the effect of reflection suppression will be limited. This is the reason why the low-frequency noise could not be handled perfectly when applying the improved method.

Therefore, we consider introducing the reflection-coefficient function according to the dip angle of structures into the non-reflecting wave equation. After obtaining the wavefield information of each time step, incident angle prediction can be performed according to the characteristics of geological continuity. Then the incident angle can be substituted into the reflection coefficient calculation process to realize the angle-adaptive RTM iterative algorithm. The RTM method based on the angle-adaptive non-reflecting wave equation would afford better low-frequency noise suppression effect in theory.

CONCLUSIONS

Low-frequency noise arising in reverse-time migration (RTM) are mainly caused by wrong cross-correlation of reflections. We attempted to suppress low-frequency noise in the process of wavefield simulation. We proposed an improved acoustic RTM based on the non-reflecting wave equation for prestack data processing. The non-reflecting wave-equation was introduced to RTM to suppress reflections in reverse simulations. Then, low-frequency noise produced by reflections could be suppressed during the application of cross-correlation imaging conditions. The method could achieve the purpose of suppressing low-frequency noise in RTM. Furthermore, the computational efficiency and storage were almost unaffected compared with the conventional method.

REFERENCES

Araya-Polo, M., Rubio, F., De la Cruz, R., Hanzich, M., Cela, J.M. and Scarpazza, D.P., 2009. 3D seismic imaging through reverse-time migration on homogeneous and heterogeneous multi-core processors. Scientif. Program., 17: 185-198.

Baysal, E., Kosloff, D.D. and Sherwood, J.W., 1983. Reverse time migration. Geophysics, 48: 1514-1524.

Baysal, E., Kosloff, D.D. and Sherwood, J.W.C., 1984. A two-way nonreflecting wave equation. Geophysics, 49: 132-141.

Bérenger, J.P., 2007. Perfectly matched layer (PML) for computational electromagnetics. Synth. Lect. Computat. Electromagn., 2: 1-117.

Brougois, A., Bourget, M., Lailly, P., Poulet, M., Ricarte, P. and Versteeg, R., 1990. Marmousi, model and data. EAEG workshop - Practical aspects of seismic data inversion (cp-108).

Chang, W.F. and McMechan, G.A.,1987. Elastic reverse-time migration. Geophysics, 52: 1365-1375.

Chattopadhyay, S. and McMechan, G.A., 2008. Imaging conditions for prestack reverse-time migration. Geophysics, 73(3), S81-S89.

Chen, T. and He, B.S., 2014. A normalized wavefield separation cross-correlation imaging condition for reverse time migration based on Poynting vector. Appl. Geophys., 11: 158-166.

Chen, Y., Bai, M., Zhou, Y., Zhang, Q., Wang, Y. and Chen, H., 2019. Substituting smoothing with low-rank decomposition - Applications to least-squares reverse time migration of simultaneous source and incomplete seismic data. Geophysics, 84(4): S267-S283.

Claerbout, J.F., 1971. Toward a unified theory of reflector mapping. Geophysics, 36: 467-481.

Dai, W., Huang, Y. and Schuster, G.T., 2013. Least-squares reverse time migration of marine data with frequency-selection encoding. Geophysics, 78(4), S233-S242.

Drossaert, F.H. and Giannopoulos, A., 2007. A nonsplit complex frequency-shifted PML based on recursive integration for FDTD modeling of elastic waves. Geophysics, 72(2): T9-T17.

Du, X., Yang, H. and Zhang, S., 2002. Wave-transmitting problem of complex structure of embankment simulated by nonreflecting wave equation. J. Tsinghua Univ., Nat. Sci. Ed. (in Chinese), 42(8): 105-108.

Fisher, E., McMechan, G.A., Annan, A.P. and Cosway, S.W., 1992. Examples of reverse-time migration of single-channel, ground-penetrating radar profiles. Geophysics, 57: 577-586.

Fletcher, R.P., Du, X. and Fowler, P.J., 2009. Reverse time migration in tilted transversely isotropic (TTI) media. Geophysics, 74(6): WCA179-WCA187.

Foltinek, D., Eaton, D., Mahovsky, J., Moghaddam, P. and McGarry, R., 2009. Industrial-scale reverse time migration on GPU hardware. Expanded Abstr., 79th Ann. Internat. SEG Mtg., Houston: 2789-2793.

Fowler, P.J., 1997. A comparative overview of prestack time migration methods. Expanded Abstr., 67th Ann. Internat. SEG Mtg., Dallas: 1571-1574.

Guitton, A., 2005. Multiple attenuation in complex geology with a pattern-based approach. Geophysics, 70(4), V97-V107.

Kaelin, B. and Guitton, A., 2006. Imaging condition for reverse time migration. Expanded Abstr., 76th Ann. Internat. SEG Mtg., New Orleans: 2594-2598.

Kang, W. and Cheng, J., 2012. Methods of suppressing artifacts in prestack reverse time migration. Progress Geophys., 3.

Karazincir, M.H. and Gerrard, C.M., 2006. Explicit high-order reverse time pre-stack depth migration. Expanded Abstr., 76th Ann. Internat. SEG Mtg., New Orleans: 2353-2357.

Kim, Y., Shin, C., Calandra, H. and Min, D.J., 2013. An algorithm for 3D acoustic time-Laplace-Fourier-domain hybrid full waveform inversion. Geophysics, 78(4): R151-R166.

Lesage, A.C., Zhou, H., Araya-Polo, M., Cela, J.M. and Ortigosa, F., 2008. 3D reverse-time migration with hybrid finite difference-pseudospectral method. Expanded Abstr., 78th Ann. Internat. SEG Mtg., Las Vegas: 2257-2261.

Levin, S.A., 1984. Principle of reverse-time migration. Geophysics, 49: 581-583.

Liu, F., Zhang, G., Morton, S.A. and Leveille, J.P., 2007. Reverse-time migration using one-way wavefield imaging condition. Expanded Abstr, 77th Ann. Internat. SEG Mtg., San Antonio: 2170-2174.

Liu, H., Liu, H. and Zou, Z., 2010. The problems of denoise and storage in seismic reverse time migration. Chin. J. Geophys., 53: 2171-2180.

Loewenthal, D. and Mufti, I.R.,1983. Reversed time migration in spatial frequency domain. Geophysics, 48: 627-635.

McMechan, G.A., 1983. Migration by extrapolation of time-dependent boundary values. Geophys. Prosp., 31: 413-420.

Mehta, K., Bakulin, A., Sheiman, J., Calvert, R. and Snieder, R., 2007. Improving the virtual source method by wavefield separation. Geophysics, 72(4): V79-V86.

Ren, C., Song, G. and Tian, X., 2015. The use of Poynting vector in wave-field decomposition imaging condition for reverse-time migration. J. Appl. Geophys., 112: 14-19.

Sava, P. and Poliannikov, O., 2008. Interferometric imaging condition for wave-equation migration. Geophysics, 73(2): S47-S61.

Sava, P. and Fomel, S., 2006. Time-shift imaging condition in seismic migration. Geophysics, 71(6): S209-S217.

Shapiro, R., 1970. Smoothing, filtering, and boundary effects. Rev. Geophys., 8: 359-387.

Suh, S.Y. and Cai, J., 2009. Reverse-time migration by fan filtering plus wavefield decomposition. Expanded Abstr., 79th Ann. Internat. SEG Mtg., Houston: 2804-2808.

Symes, W.W., 2007. Reverse time migration with optimal checkpointing. Geophysics, 72(5), SM213-SM221.

Valenciano, A.A. and Biondi, B., 2003. 2-D deconvolution imaging condition for shot-profile migration. Expanded Abstr., 73rd Ann. Internat. SEG Mtg., Dallas: 1059-1062..

Verschuur, D.J. and Berkhout, A. J., 1997. Estimation of multiple scattering by iterative inversion, Part II: Practical aspects and examples. Geophysics, 62: 1596-1611.

Wang, D., Saab, R., Yilmaz, Ö. and Herrmann, F.J., 2008. Bayesian wavefield separation by transform-domain sparsity promotion. Geophysics, 73(5): A33-A38.

Wang, S. and Qu, Y., 1993. Mixed two-way nonreflecting wave equation migration. Petrol. Geophys. Explor. (in Chinese), 28: 537-542.

Wang, Y., 2000. Reverse-time migration by a variable time-step and space-grid method. Expanded Abstr., 70th Ann. Internat. SEG Mtg., Calgary, AB: 798-801.

Wang, Y., Zhou, H., Chen, H. and Chen, Y., 2018. Adaptive stabilization for Q-compensated reverse time migration. Geophysics, 83(1): S15-S32.

Whitmore, N.D., 1983. Iterative depth migration by backward time propagation. Expanded Abstr., 53rd Ann. Internat. SEG Mtg., Las Vegas: 382-385.

Wu, Q., Li, W., Chen, K. and Cui, J., 2000. Forward model of nonreflecting wave equation and its application. Petrol. Geophys. Explor. (in Chinese), 35: 147-153.

Xu, K., Zhou, B. and McMechan, G.A., 2010. Implementation of prestack reverse time migration using frequency-domain extrapolation. Geophysics, 75(2): S61-S72.

Xue, Z., Chen, Y., Fomel, S. and Sun, J., 2016. Seismic imaging of incomplete data and simultaneous-source data using least-squares reverse time migration with shaping regularization. Geophysics, 81(1): S11-S20.

Yoon, K., Marfurt, K.J. and Starr, W., 2004. Challenges in reverse-time migration. Expanded Abstr., 74th Ann. Internat. SEG Mtg., Denver: 1057-1060.

Youn, O.K. and Zhou, H.W., 2001. Depth imaging with multiples. Geophysics, 66(1): 246-255.

Zhang, W. and Shen, Y., 2010. Unsplit complex frequency-shifted PML implementation using auxiliary differential equations for seismic wave modeling. Geophysics, 75(4): T141-T154.

Zhang, Y. and Zhang, G., 2009. One-step extrapolation method for reverse time migration. Geophysics, 74(4): A29-A33.

Zhu, J., Dong, M. and Li, C., 1989. The vsp's reverse-time migration based on two-way nonreflecting wave equation. Petrol. Geophys. Explor. (in Chinese), 24: 256-270.

Zhu, T. and Sun, J., 2017. Viscoelastic reverse time migration with attenuation compensation. Geophysics, 82(2): S61-S73.